

# Histopathology for Mohs Micrographic Surgery with Photoacoustic Remote Sensing Microscopy

BENJAMIN R. ECCLESTONE,<sup>1</sup> KEVAN BELL,<sup>1,2</sup> SAAD ABBASI,<sup>1</sup> DEEPAK DINAKARAN,<sup>2,3</sup> MUBA TAHER,<sup>4</sup> JOHN R. MACKEY,<sup>2,3</sup> PARSIN HAJI REZA<sup>1,\*</sup>

<sup>1</sup>*PhotoMedicine Labs, Department of Systems Design Engineering, University of Waterloo, 200 University Ave W, Waterloo, Ontario, N2L 3G1, Canada*

<sup>2</sup>*illumiSonics, Inc., Department of Systems Design Engineering, University of Waterloo, 200 University Ave W, Waterloo, Ontario, N2L 3G1, Canada*

<sup>3</sup>*Department of Oncology, University of Alberta, 8440 112 St. NW, T6G 2R7, Edmonton, Alberta, Canada*

<sup>4</sup>*Division of Dermatology, Department of Medicine, University of Alberta, 116 St & 85 Ave, Edmonton, Alberta, T6G 2V1, Canada*

[\\*phajireza@uwaterloo.ca](mailto:phajireza@uwaterloo.ca)

**Abstract:** Mohs micrographic surgery (MMS) is a precise technique where layers of tissue are resected and examined with intraoperative histopathology to minimize the removal of normal tissue while completely excising the cancer. To achieve intraoperative pathology, the tissue is frozen, sectioned and stained over a 20- to 60-minute period, then analyzed by the MMS surgeon. Surgery is continued one layer at a time until no cancerous cells remain, meaning MMS can take several hours to complete. Ideally, it would be desirable to circumvent or augment frozen sectioning methods and directly visualize subcellular morphology on the unprocessed excised tissues. Employing photoacoustic remote sensing (PARS<sup>TM</sup>) microscopy, we present a non-contact label-free reflection-mode method of performing such visualizations in frozen sections of human skin. PARS leverages endogenous optical absorption contrast within cell nuclei to provide visualizations reminiscent of histochemical staining techniques. Here, we demonstrate the ability of PARS microscopy to provide large grossing scans ( $>1\text{ cm}^2$ , sufficient to visualize entire MMS sections) and regional scans with subcellular lateral resolution ( $400 \pm 150\text{ nm}$ ).

## 1. Introduction

Mohs micrographic surgery (MMS) is the gold standard precision surgical technique for treating contiguous invading skin cancers in cosmetically and functionally important areas [1]. MMS excision of nonmelanoma skin cancers (NMSC) represents one of the most common procedures in the United States. Around 25% of the 3.5 million NMSC cases diagnosed each year are treated with this procedure [2,3]. In recent years NMSC incidence has risen dramatically, straining the global capacity to provide MMS [2]. For the two most common NMSCs, basal cell carcinomas (BCC) and squamous cell carcinomas (SCC), MMS achieves a five-year cure rate of nearly 99% [4,5]. For high risk nonmelanoma lesions, MMS achieves higher cure rates than wide local excision [6-8]. MMS repeatedly excises thin tissue layers that then undergo intraoperative histopathological analysis to identify regions of invasion at the margins. During MMS, the surgeon will excise successive shallow layers of tissue capturing a 2 to 3 mm margin around the tumor [9]. The excised tissue sample undergoes frozen sectioning and histochemical staining to permit transmission light microscopic assessment. In contrast to other surgical techniques, in MMS the entire deep and peripheral margin of the excised tissue undergoes pathological analysis. By assessing the entire surgical margin in this manner, the surgeon is able to identify specific invasive regions of malignant cells. This process of layer by layer excision with interim histopathological analysis is repeated until the entire invasive tumor has been removed [9].

The use of intraoperative frozen histology means operating times for MMS can exceed several hours, depending on the number of excisions required [10]. Most of this time is consumed by tissue processing, which requires 30 to 60 minutes per tissue layer, while the excision and pathologic assessment are relatively rapid [9]. Consequently, the rate limiting step in the MMS process is generating the tissue suitable for transmission light microscopic interpretation. The MMS process could be accelerated greatly if tissue processing could be circumvented, and unstained tissues visualized directly. Ideally, images so obtained would be visually similar to standard histochemical staining images. Furthermore, this would also preserve sample integrity permitting re-examination and additional immunochemistry analysis.

Direct histological imaging of unstained tissue sections presents unique challenges compared to pathological analysis of stained frozen preparations. Nonetheless, a variety of imaging methods have demonstrated histology-like imaging in MMS excisions. Prominent examples include microscopy with ultraviolet surface excitation (MUSE) [11], multiphoton fluorescence microscopy (MPM) [12,13], Raman spectroscopy [14-16], photoacoustic microscopy (PAM) [17,18], and optical coherence tomography (OCT) [19-21], each of which has been explored for intraoperative histology for MMS. While MUSE and MPM have shown promising histology-like images, they require exogenous dyes for contrast. Staining tissues prior to imaging reintroduces many of the tissue preparation issues experienced by frozen histology, as staining can be resource intensive and complex, and introduces a potential for variability. Of the above techniques then, Raman spectroscopy, PAM and OCT are the only modalities demonstrating label-free histology-like imaging of MMS specimens [14-21].

Considering the potential imaging techniques, PAM [17,18], Raman spectroscopy [14-16] and OCT [19-21] histopathology all provide resolutions significantly inferior to conventional optical microscopy. Applied in-vivo, both PAM [17,18] and Raman spectroscopy [14-16] fail to provide subcellular resolution. Hence, both techniques are inadequate for precisely locating small and subtle regions of malignant cells. These modalities are then inappropriate for MMS where nuclear morphology of the entire deep and peripheral margin of the excised tissue must be assessed. While OCT, provides subcellular resolution the optical scattering contrast in OCT does not provide the specificity necessary to match current pathology standards [19-21]. To provide visualizations reminiscent of current H&E staining, OCT systems must use external image processing techniques. Therefore, there remains a pressing need for an accurate

interoperative label-free histopathological microscopy technique capable of imaging large areas of tissue while also providing subcellular resolution to expedite MMS procedures.

Photoacoustic Remote Sensing (PARS<sup>TM</sup>) microscopy has recently emerged as an all-optical non-contact label-free reflection-mode imaging modality [22-24]. Like other photoacoustic techniques, PARS captures endogenous optical absorption contrast visualizing a wide range of biological chromophores including hemoglobin, lipids, and DNA. A pulsed excitation laser is used to deposit optical energy into the sample. As the target chromophore absorbs the excitation pulse, it undergoes thermo-elastic expansion proportional to the absorbed excitation energy. The expansion induces nanosecond scale modulations in the local refractive index of the sample. In PARS, this effect is observed as back-reflected intensity variations of a second co-focused continuous-wave detection laser. In this way, PARS microscopy visualizes endogenous absorption contrast in an all-optical label-free reflection-mode architecture [22-24]. Previously, our group has shown promising histology-like imaging capabilities by utilizing ultraviolet excitation to primarily target the absorption contrast of DNA [23,24]. Accentuating this contrast generates visualizations reminiscent of immunohistochemical staining of cell nuclei. In recent works, PARS histological imaging has been applied in thick tissue samples (>2 mm) including freshly resected tissues and formalin fixed paraffin embedded tissue preparations [23,24].

In this work, we present a PARS system for rapid label-free histological imaging of unprocessed MMS sections. By leveraging recent technical improvements of the PARS system, we have expanded the histological imaging capabilities to match the scanning area, resolution and imaging speed required for MMS. We show the first non-contact photoacoustic microscopy of Mohs excisions. Wide field of view grossing scans capture entire MMS sections (>1 cm<sup>2</sup> area) with sufficient resolution to recover subcellular diagnostic characteristics. Concurrently, smaller high-resolution images give close-ups of clinically relevant regions. These small fields provide  $400 \pm 150$  nm optical resolution enabling morphological assessment of single nuclei. Thus, the proposed PARS system provides both the grossing scan capabilities, and high spatial resolution required to assess tissues during MMS. Compared to frozen histology, the presented PARS microscope without optimized scanning hardware can image an entire MMS excision in under 12 minutes, 60% of the time for standard MMS tissue preparation. Applied in a clinical setting, this device may circumvent the need for histopathological processing of tissue. Thus, PARS is well positioned to supplement existing intraoperative tissue analysis techniques, potentially reducing the time for each MMS operative cycle, streamlining the MMS process, thereby increasing MMS capacity.

## **2. Methods**

### **2.1 *Imaging System:***

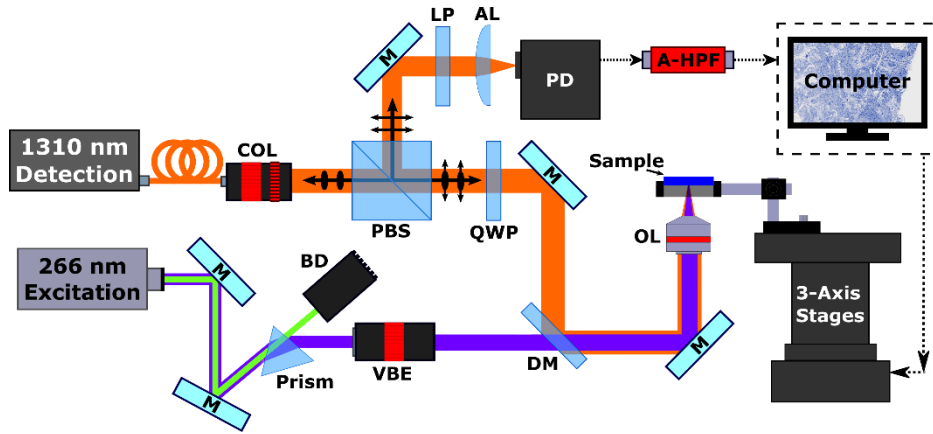


Fig. 4. Simplified Schematic of the PARS system. Component labels are defined as follows: collimator (COL), polarizing beam splitter (PBS), quarter wave plate (QWP), dichroic mirror (DM), variable beam expander (VBE), beam dump (BD), objective lens (OL), long pass filter (LP), aspheric focal lens (AL), photodiode (PD), analogue high-pass filter (A-HPF), mirrors (M).

The proposed imaging system is shown in Figure 1. A 400 ps pulsed laser (WEDGE XF, Bright Solutions) was selected to provide 266 nm UV excitation. Residual 532 nm output is removed from the excitation beam with a CAF2 prism (PS862, Thorlabs). Following separation, the UV beam is expanded (BE05-266, Thorlabs) and combined with the detection beam via dichroic mirror (HBSY234, Thorlabs). Detection of PARS signals is performed with a 1310 nm continuous wave super-luminescent diode (S5FC1018P, Thorlabs). Collimated, horizontally polarized detection light passes through a polarizing beam splitter (PBS254, Thorlabs) and quarter wave plate (WPQ10M-1310, Thorlabs) into the imaging system. Both excitation and detection are then co-focused onto the sample with a 0.5 NA reflective objective (LMM-15X-UVV, Thorlabs). The back reflected detection beam from the sample which encodes the PARS modulations, is returned along detection pathway. Passing through the quarter wave plate for a second time, the detection beam becomes horizontally polarized. The horizontally polarized light is then directed towards the photodetector by the polarizing beam splitter where it is filtered (FELH1000, Thorlabs) before being focused onto the photodiode (PDB425C-AC, Thorlabs).

Images were collected by mechanically scanning samples over the fixed imaging head in a continued raster pattern. While scanning, the excitation laser pulses continually capturing evenly spaced PARS interrogation points. The lateral spacing between PARS collection points is then tuned by adjusting the stage speed and excitation laser repetition rate. Depending on the desired resolution, the lateral spacing ranged from 0.1 to 5  $\mu\text{m}$ . Each time the excitation laser is pulsed, a short segment of photodetector signal is recorded capturing the PARS modulations. To ensure accurate recovery of the PARS interrogation, around 250 samples of the photodiode signal are captured with a 14-bit digitizer (RZE-004-300, Gage Applied). This time domain data is streamed via PCI-E channel from the digitizer to the computer memory. Here, an algorithm was applied to extract the characteristic amplitude of each PARS signal in real time. The image is then reconstructed by imposing the collected data on a Cartesian grid [23,24].

## 2.2 Sample Preparation:

In this study, a variety of MMS excisions with BCC were selected for imaging. Frozen sections of tissue specimens with BCC were obtained from Mohs surgeries. The Mohs

excisions are embedded within a cutting substrate and placed into a cryostat where they are cooled to approximately  $-25^{\circ}\text{C}$ , over a 1 to 10-minute period (depending on sample shape and composition). The frozen samples were then sectioned via cryotome into 5-10-micron slices and placed onto a microscope slide. The slide was then dried and fixed at  $55^{\circ}\text{C}$  for 1 minute. Two sections were collected and fixed from each tissue sample, the outermost section was stained with toluidine blue, while the inner section was kept unstained. The toluidine blue staining was performed with 1% toluidine blue aqueous solution, a standard protocol for BCC. Once stained, the slides were covered with mounting media. The tissue samples were collected under protocols approved by the Research Ethics Board of Alberta (Protocol ID: HREBA.CC-18-0277) and the University of Waterloo Health Research Ethics Committee (Humans: #40275). The ethics committees waived the requirement for patient consent as the selected samples were excess tissues no-longer required for diagnostic purposes, and no patient identifiers were provided to the researchers. All experiments were performed in accordance with the requirements of the Government of Canada Panel on Research Ethics Guidelines.

### 3. Results and Discussion

Results of large grossing scans are shown in Figure 2. Figure 2a and 2b feature large field of view scans of a human MMS excision with BCC (13 mm and 10 mm side lengths respectively). In each case, dense regions of tumor tissues are observed within the excised tissues. Moreover, the bulk tissue morphology and the surgical margins can be assessed readily. A region of hypercellularity is seen extending and infiltrating into normal skin tissue (Figure 2a). Further resection layer shows only normal skin tissue (Figure 2b) with hair follicles being visible.

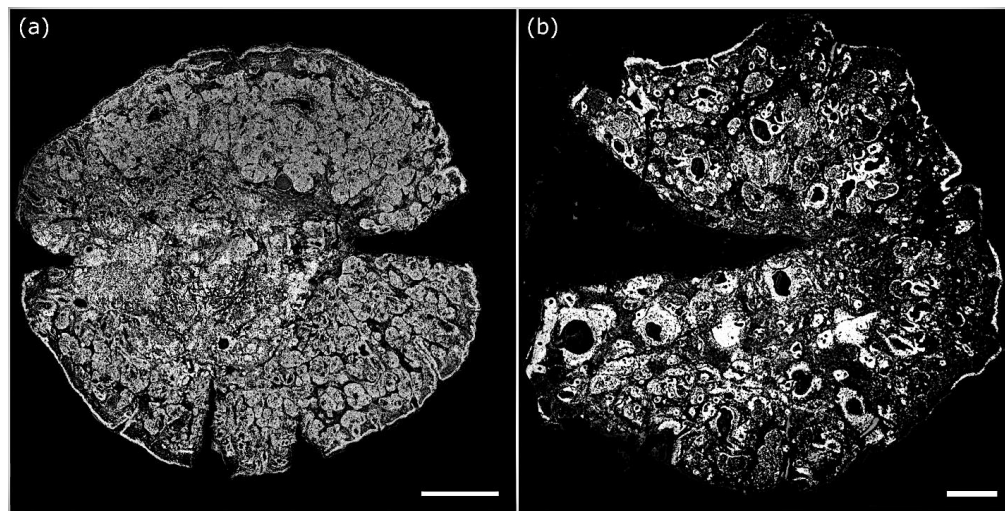


Fig. 2. Wide field of view PARS images of entire Mohs excisions. a) 13 mm by 13 mm PARS image of human skin tissue with basal cell carcinoma shown by the increased cellularity in the middle (deep) margin causing invasion and architectural distortion of the normal skin (scale Bar: 2 mm). b) 10 mm by 10 mm PARS image of human skin tissue (scale Bar: 1 mm). Both a & b feature a  $4\text{ }\mu\text{m}$  lateral step size.

Assessing the entire excision surface is crucial to the high success of MMS compared to other techniques. Observing the entire surgical margin means areas of contiguous invasion can be identified for excision. By necessity, tissue sections exceeding  $1.0\text{ cm}^2$  in area, such as the scans presented in Figure 2, must be imaged with subcellular resolution. Moreover, to improve on frozen sectioning, imaging must be performed in under 20 minutes. Ideally the imaging time

should be further reduced, to under 10 minutes. Several technical improvements have been made over previous reports of PARS devices to match the scanning area, resolution and imaging speed required for MMS. These have included improvements to scanning accuracy, imaging speed, image reconstruction techniques, data management, and system sensitivity. By the nature of the point scanning mechanism, these improvements have enhanced both the grossing scans and small field scans. At each scale, (large or small scan window) the number of interrogation points may remain the same, however, the excitation rate and/or mechanical scanning speed may be scaled up or down to provide the desired lateral step size and resolution.

Increasing the scan area is usually accompanied by a corresponding reduction in resolution or an increase in acquisition time. Fortunately, in PARS, the impacts on resolution and imaging speed may be mostly mitigated by selecting a sufficiently high excitation laser repetition rate. However, increasing the repetition rate while maintaining the same spatial sampling rate also necessitates an increase in the movement speed of the scanning stages. In the proposed system, these stages are limited to a maximum velocity of 200 mm/s. Thus, for the grossing scans displayed in Figure 2 a and b, maintaining 4  $\mu\text{m}$  spatial sampling requires a repetition rate of 50 kHz. Operating at the maximum mechanical velocity and 50 kHz excitation, a 16-million-point scan similar to Figure 3, or Figure 4, could be captured in roughly 12 minutes. Moving forwards, the imaging time will be drastically reduced by exchanging the mechanical stages and excitation laser. Utilizing a commercially available 600 mm/s mechanical stage in conjunction with a 1 MHz excitation would reduce the imaging time from 12, to under 2 minutes. However, another issue arises as capturing images such as Figure 2, or Figure 3 (16-million-points/image) would potentially result in nearly 30 GB of data for a single capture. To circumvent this issue, an algorithm was applied to extract the characteristic amplitude of each PARS signal in real time. Thus, the memory requirement is reduced by around 256 times. As a result, the number of PARS signals which can be reasonably recovered in a single scan is increased by the same factor, enabling practical acquisition of the presented larger and/or higher resolution scans.

Compared to the wide field images in Figure 2, the tighter spatial sampling and smaller field of view in Figure 3 reveal more intricate tissue morphology. By reducing the lateral spatial sampling rate to 250 nm, we achieve an optically limited resolution of  $400 \pm 150$  nm. Presented in Figure 3 is a series of high-resolution PARS images of a tissue sample with BCC (bottom (ii)). Images of a similar tissue region prepared with standard frozen histology sectioning and toluidine blue staining are shown across the top row (i) of Figure 3. The toluidine blue dye in Figure 3 is commonly used in MMS for assessing NMSC. It should be noted that while the unstained and stained slices are adjacent, there are differences in bulk structure as these sections are 5-10  $\mu\text{m}$  thick. Within the images, the margin of invasive disease is identified due to high cellularity and corresponding nuclear content on PARS imaging, which corresponds to the light microscopy images. The nuclear atypia and disorganized cellular organization are indicative of the presence of cancerous tissue.

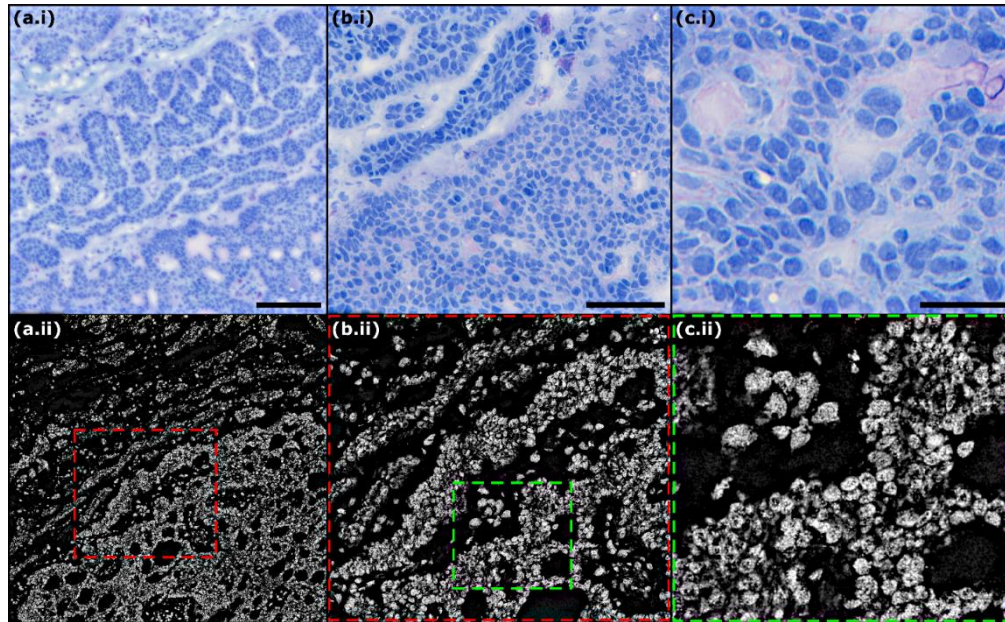


Fig.3 Comparison of PARS and bright-field images of toluidine blue (TB) stained human skin tissue with basal cell carcinoma (BCC). a) (i) 5x bright field image of tissue with BCC. (ii) PARS image of an adjacent unstained sample with BCC. Scale Bar: 200  $\mu\text{m}$  b) (i) 20x bright field image demonstrating the border of invasive cancer (bottom) versus normal tissue (top). (ii) Enlarged section (red box) of the PARS image (a.ii) compares the disorganized cellular architecture seen in the light microscopy and PARS images. Scale Bar: 100  $\mu\text{m}$  c) (i) 20x bright field of tissue with clearly identifiable atypical nuclear morphology, size and distribution. (ii) Enlarged section (green box) of the PARS image (b.ii). Scale Bar: 40  $\mu\text{m}$ . NOTE: While the unstained and stained slices are adjacent, there are differences in bulk structure as the sections are 5-10  $\mu\text{m}$  thick.

Presented in Figure 4a is a series of 4 smaller 1 mm<sup>2</sup> images co-registered to form a 4 mm x 1 mm image with resolution equivalent to Figure 3. Each individual frame is 28 megapixels, 4000 by 7000-point image. Shown in this image is the transition from cancerous tissue to normal tissue at the tumor margin. The ability to identify this tumor margin will guide the MMS surgeon in resecting the next layer of tissue.



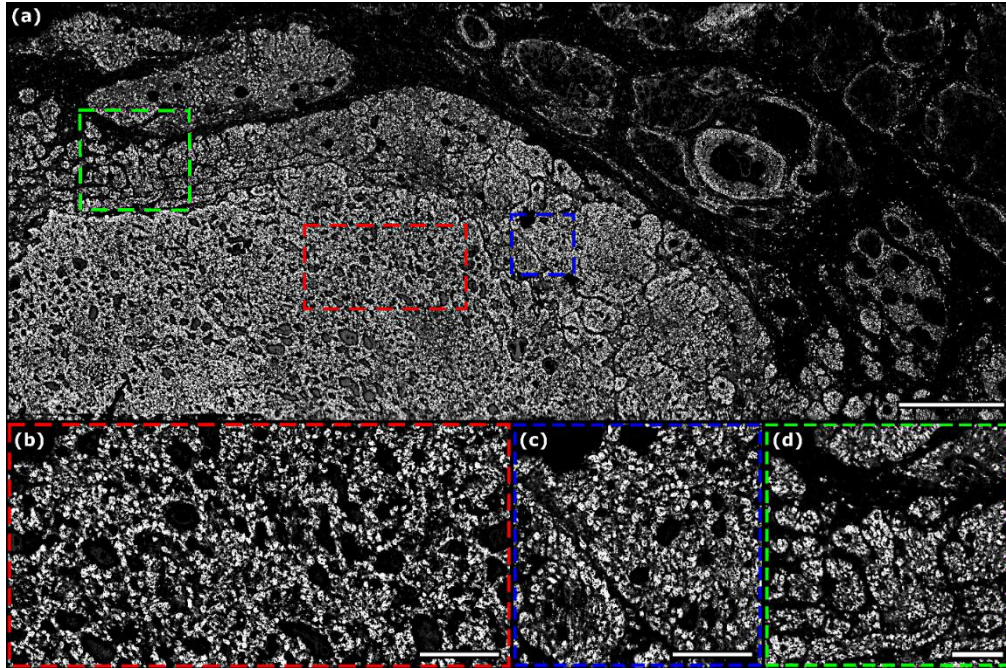


Fig. 4. Large area high resolution PARS image of human skin tissue with basal cell carcinoma. (a) A series of four PARS images stitched together (112-megapixel image, 16000 by 7000-point scan, 250 nm step size) with hypercellularity and nuclear content giving high PARS signal along with evident disorganized cellular architecture denoting cancerous tissue seen in the bottom left and normal tissue in the top and right. Scale Bar: 400  $\mu\text{m}$  (b) Cropped and enlarged section (red box) of the PARS image shown in (a) Scale Bar: 100  $\mu\text{m}$  (c) Cropped and enlarged section (blue box) of the PARS image shown in (a) Scale Bar: 100  $\mu\text{m}$  (d) Cropped and enlarged section (green box) of the PARS image shown in (a) Scale Bar: 100  $\mu\text{m}$

While the UV absorption of DNA is orders of magnitude higher than surrounding chromophores, most common biomolecules have non-zero optical absorption of UV. As a result, subtle contrast attributed to biomolecules, such as cytochrome, hemoglobin and collagen can be recovered by applying non-linear scaling to the absorption data. Such extranuclear details are observed in Figure 4. To accentuate these subtle details, the PARS optical system was refined to ensure maximum detection sensitivity. While these refinements have enhanced non-nuclear contrast, the extranuclear chromophores cannot be individually identified as their UV absorptions are relatively similar. However, recovering bulk tissue contrast from extranuclear structures still imparts a visualization benefit, as bulk tissue morphology may be captured in addition to nuclear contrast with a single wavelength. Moving forward, additional chromophore specific excitation wavelengths will be explored. Rather than using UV excitation, the infra-red absorption of DNA may be targeted to provide similar histology-like contrast while improving in-situ compatibility. Additionally, further excitation wavelengths will be added providing selective contrast for biomolecules such as lipids and collagen.

In addition to adding more chromophore specificity, future works will focus on increasing imaging speed. Considering the current system, capturing a single grossing or small region scan requires around 12 minutes and provides a 16-megapixel image. This is approximately 60% the time required for frozen histology preparation. However, to recover wider swaths such as Figure 4a, the scanning time increases linearly with 4 frames requiring 48 minutes. While still comparable to frozen sectioning, the PARS imaging time exceeds that of frozen pathology depending on how many scans are required. Moving forward, the imaging speed may be improved by increasing the point capture/excitation rate. Previous works have reported



excitation rates of nearly 1 MHz, which if employed, would reduce imaging time to less than 30 seconds per scan [25]. Concurrently, to avoid mechanical limitations, more efficient scanning methods will be implemented. Future work will focus on incorporating these improvements aiming to image entire MMS excisions in one capture, with the same area as the presented grossing scans (Figure 2), and the same spatial sampling as the presented high-resolution captures (Figure 3 and Figure 4).

#### **4. Conclusion**

In summary, incorporating the PARS system improvements discussed here have thus far enabled an increase in imaging area, repeatability, sensitivity, and resolution. The presented results demonstrate the first visualization of nuclear morphology in human tissue samples exhibiting BCC, using a non-contact photoacoustic microscopy technique. Shown here, subcellular structures are recovered from entire MMS sections, enabling full tissue margin analysis. Concurrently, small regions are captured providing close-ups of clinically relevant features such as nuclear organization, density and morphology. The current PARS system facilitates recovery of these details more rapidly than conventional processing techniques by eliminating tissue processing steps. PARS emulates the contrast provided by common histochemical stains, suggesting that if adopted, there may be little requirement to retrain pathologists to interpret a new image type. Moreover, the non-contact label-free reflection-mode PARS microscope presented here, could potentially be applied directly to unprocessed MMS excisions. This suggests bulk tissues could be preserved in their entirety enabling re-examination, further histopathological processing and immunochemistry. Thus, this device may circumvent the need for frozen pathology, or could act as an adjunct to the current processing stream. Overall, the PARS modality is well suited to intraoperative guidance of MMS and could reduce MMS cycle time, increase patient flow, and free up histopathology staff to perform other tasks. Moving forwards, the performance of this system will be examined in freshly resected, bulk MMS excisions.

#### **Funding**

Natural Sciences and Engineering Research Council of Canada (DGEER-2019-00143, RGPIN2019-06134); Canada Foundation for Innovation (JELF #38000); Mitacs Accelerate (IT13594); University of Waterloo Startup funds; Centre for Bioengineering and Biotechnology (CBB Seed fund); illumiSonics Inc (SRA #083181); New frontiers in research fund – exploration (NFRFE-2019-01012).

#### **Acknowledgments**

N/A

#### **Disclosures**

KB: illumiSonics Inc. (F, I, E, P); DD: illumiSonics Inc. (I); JRM: illumiSonics Inc. (I); PHR: illumiSonics Inc. (F, I, P, S).

#### **5. References**

1. E.M. Finley, "The principles of mohs micrographic surgery for cutaneous neoplasia," *Ochsner. J.* **5**(2), 22-33 (2003).

2. E. Perera and R. Sinclair, "An estimation of the prevalence of nonmelanoma skin cancer in the U.S. F1000Res," **2**,107 (2013).
3. J.T. Chen, S.J. Kempton, and V.K. Rao, "The Economics of Skin Cancer: An Analysis of Medicare Payment Data," *Plast. Reconstr. Surg. Glob.* **4**, e868. (2016).
4. D.E. Rowe, R.J. Carroll and C.L. Day, "Long-term recurrence rates in previously untreated (primary) basal cell carcinoma: Implications for patient follow-up," *J. Dermatol. Surg. Oncol.* **15**(3), 315–328 (1989).
5. D.E. Rowe, R.J. Carroll, C.L. Day, "Prognostic factors for local recurrence, metastasis, and survival rates in squamous cell carcinoma of the skin, ear, and lip. Implications for treatment modality selection," *J. Am. Acad. Dermatol.* **26**(6), 976–990 (1992).
6. V. Samarasinghe and V. Madan, "Nonmelanoma skin cancer," *J. Cutan. Aesthet. Surg.* **5**(1), 3-10 (2012).
7. D. Beaulieu, R. Fathi, D. Srivastava, and R.I. Nijhawan, "Current perspectives on Mohs micrographic surgery for melanoma," *Clin. Cosmet. Investig. Dermatol.* **11**, 309-20 (2018).
8. M. Rajadhyaksha, G. Menaker, T. Flotte, P.J. Dwyer and S. González, "Confocal examination of nonmelanoma cancers in thick skin excisions to potentially guide mohs micrographic surgery without frozen histopathology," *J. Invest. Dermatol.* **117**(5), 1137-1143 (2001).
9. P. Gauthier, H. Ngo, K. Azar, A. Allaire, L. Comeau, C. Maari, P. Marinier, and N. Meunier, "Mohs surgery - a new approach with a mould and glass discs: review of the literature and comparative study," *J. Otolaryngol.* **35**(5), 292-304 (2006).
10. J. Cook and J. Zitelli, "Mohs micrographic surgery: A cost analysis," *J. Am. Acad. Dermatol.* **39**, 698-703 (1998).
11. T. Yoshitake, M.G. Giacomelli, L.M. Quintana, H. Vardeh, L.C. Cahill, B.E. Faulkner-Jones, J.L. Connolly, D. Do and J.G. Fujimoto, "Rapid histopathological imaging of skin and breast cancer surgical specimens using immersion microscopy with ultraviolet surface excitation," *Sci. Rep.* **8**, 4476 (2018).
12. C. Longo, M. Ragazzi, M. Rajadhyaksha, K. Nehal, A. Bennassar, G. Pellacani and J.M. Guiler, "In Vivo and Ex Vivo Confocal Microscopy for Dermatologic and Mohs Surgeons," *Dermatol. Clin.* **34**(4), 497-504 (2016).
13. J. Paoli, M. Smedh, A. Wennberg and M.B. Ericson, "Multiphoton Laser Scanning Microscopy on Non-Melanoma Skin Cancer: Morphologic Features for Future Non-Invasive Diagnostics," *J. Invest. Dermatol.* **128** (5), 1248-1255 (2008).
14. M. Larraona-Puy, A. Ghita, A. Zoladek, W. Perkins, S. Varma, I.H. Leach, A.A. Koloydenko, H. Williams and I. Notingher, "Discrimination between basal cell carcinoma and hair follicles in skin tissue sections by Raman micro-spectroscopy," *J. Mol. Struct.* **993**(3), 57-61 (2011).
15. K. Kong, C.J. Rowlands, S. Varma, W. Perkins, I.H. Leach, A.A. Koloydenko, A. Pitiot, H.C. Williams, and I. Notingher, "Increasing the speed of tumour diagnosis during surgery with selective scanning Raman microscopy," *J. Mol. Struct.* **1073**, 58-65 (2014).
16. C.A. Lieber, S.K. Majumder, D.L. Ellis, D.D. Billheimer and A. Mahadevan-Jansen, "In vivo nonmelanoma skin cancer diagnosis using Raman microspectroscopy," *Lasers. Surg. Med.* **40**(7), 461-467 (2008).
17. U. Dahlstrand, R. Sheikh, A. Merdasa, R. Chakari, B. Persson, M. Cinthio, T. Erlov, B. Gesslein, and M. Malmström, "Photoacoustic imaging for three-dimensional visualization and delineation of basal cell carcinoma in patients," *Photoacoustics*. **18**, 100187 (2020).
18. A.B.E. Attia, S.Y. Chuah, D. Razansky, C. Jun Hui Ho, P. Malempati, U.S. Dinish, R. Bi, C. Yaw Fu, S.J. Ford, J. Siong See Lee, M.W. Ping Tan, M. Olivo, and S. Tien Guan Thng, "Noninvasive real-time

characterization of non-melanoma skin cancers with handheld optoacoustic probes,” *Photoacoustics*. **7**, 20-26 (2017).

19. S.A. Alawi, M. Kuck, C. Wahrlich, S. Batz, G. McKenzie, J.W. Fluhr, J. Lademann and M. Ulrich, “Optical coherence tomography for presurgical margin assessment of non-melanoma skin cancer – a practical approach,” *Exp. Dermatol.* **22**(8), 547-551 (2003).
20. D. Rashed, D. Shah, A. Freeman, R.J. Cook, C. Hopper and C.M. Perrett, “Rapid ex vivo examination of Mohs specimens using optical coherence tomography,” *Photodiagnosis. Photodyn. Ther.* **19**, 243-248 (2017).
21. C.S. Chan, T.E. Rohrer. “Optical Coherence Tomography and Its Role in Mohs Micrographic Surgery: A Case Report,” *Case. Rep. Dermatol.* **4**(3), 269-274 (2012).
22. P. Haji Reza, W. Shi, K. Bell, P. Paproski, and R.J. Zemp, “Non-interferometric photoacoustic remote sensing microscopy,” *Light. Sci. Appl.*, **6**, e16278 (2017).
23. S. Abbasi, M. Le, B. Sonier, K. Bell, D. Dinakaran, G. Bigras, J.R. Mackey and P. Haji Reza, “Chromophore selective multi-wavelength photoacoustic remote sensing of unstained human tissues,” *Biomed. Opt. Express*. **10**(11), 5461-5469 (2019).
24. S. Abbasi, M. Le, B. Sonier, D. Dinakaran, G. Bigras, K. Bell, J.R. Mackey and P. Haji Reza, “All-optical Reflection-mode Microscopic Histology of Unstained Human Tissues,” *Sci Rep* **9**, 13392 (2019).
25. S. Abbasi, K. Bell, B.R. Ecclestone, P. Haji Reza, “Real Time & 3D Photoacoustic Remote Sensing” in *Biophotonics Congress: Biomedical Optics 2020 (Translational, Microscopy, OCT, OTS, BRAIN), OSA Technical Digest (Optical Society of America, 2020) (2020), Poster JTh2A.13.*